Journal of Alloys and Compounds 513 (2012) 559–565

Contents lists available at SciVerse ScienceDirect

Journal of Alloys and Compounds

journal homepage: www.elsevier.com/locate/jallcom

Synthesis and spectroscopy of color tunable $Y_2O_2S:Yb^{3+},Er^{3+}$ phosphors with intense emission

G.A. Kumar[a,*], M. Pokhrel[a], A. Martinez[b], R.C. Dennis[a], I.L. Villegas[c], D.K. Sardar[a]

[a] Department of Physics and Astronomy, University of Texas at San Antonio, San Antonio, TX 78249-0697, USA
[b] Centro de Investigaciones en Optica A.C., León, Gto., 37150 México, Mexico
[c] Grupo de Espectroscopia de Materiales Avanzados y Nanoestructurados (EMANA), Centro de Investigaciones en Optica A.C., León, Gto., 37150 México, Mexico

ARTICLE INFO

Article history:
Received 17 June 2011
Received in revised form 1 November 2011
Accepted 2 November 2011
Available online 9 November 2011

Keywords:
Phosphor
Upconversion
Optical material
Luminescence
Two photon absorption
Energy transfer

ABSTRACT

Trivalent ytterbium and erbium doped in yttrium oxysulfide ($Y_2O_2S:Yb^{3+},Er^{3+}$) phosphors were synthesized by solid state flux fusion method and their upconversion spectral properties were studied as a function of different Yb^{3+} concentrations. The solid state flux fusion results in well crystallized hexagonal shaped phosphor particles with an average size of 3.8 μm. The detailed optical characterizations such as absorption, emission, and fluorescence decay were performed to explore the emission processes in the UV–VIS–NIR as well as to quantitatively estimate the fluorescence quantum yield. Upconversion spectral studies show that for all the compositions, green emissions are stronger; in particular the green emission intensity is 1.7 times stronger than the red intensity with composition of 9 mol% Yb^{3+} and 1 mol% Er^{3+}. Mechanisms of upconversion by two-photon and energy transfer processes are interpreted and explained. The color coordinates are measured and the color tunability was analyzed as a function of the 980 nm excitation power. Results show that the $Y_2O_2S:Yb^{3+},Er^{3+}$ phosphor offers power dependent color tuning properties where the emission color can be tuned from 490 to 550 nm by simply changing the 980 nm excitation power from 10 to 50 mW.

1. Introduction

Upconversion is the spectroscopic process where low energy photon of higher wavelength are converted into one or more high energy photons of lower wavelength. Spectroscopically this is happening through the multiphoton absorption process where a low energy photon is being absorbed to the higher state by multiphoton absorption. In order to have efficient two photon absorption the material should have higher multiphoton absorption coefficient and that enables the application of several organic nonlinear materials as potential candidates for efficient upconversion. However, it was found that upconversion can also occur efficiently in several trivalent rare earth doped materials. Here the upconversion is mainly happening through multiphoton absorption through real excited states through the process of excited state absorption and other energy transfer processes. Since the processes are happening through the real states the upconversion emission could be observed even at low excitation laser power and that is an added advantage of rare earth doped upconversion phosphors. At present rare earth doped upconversion phosphors find a big market in the photonics industry due to their synthesis flexibility, low cost of production, photo-stability, low toxicity and size independent optical properties [1]. The application of these phosphors could be found in several areas such as security, solid state lasers, IR detection, medical imaging, therapy, solid state displays (2D, 3D), and fiber optic amplifiers [2–4]. It is anticipated that in several biomedical and imaging applications rare earth doped materials may become an attractive alternative to organic dyes and quantum dots.

It has been found that hetero halide and heavy metal based materials offer efficient luminescence due to their low lattice vibration frequencies [5]. However, many of the halides are air sensitive as well as toxic and several could not be realized in large scale industrial applications. Chalcogenides such as S, Se, and Te, are also found to be potential candidates despite their phonon frequencies being slightly higher than halides [6]. Among chalcogenides, rare earth oxysulfides posses several excellent properties such as chemical stability and low toxicity, and can be easily mass produced at low cost. Rare earth oxysulfides have an average phonon energy of approximately 520 cm^{-1} [7]. For example, $Y_2O_2S:Yb^{3+},Er^{3+}$ and $Y_2O_2S:Er^{3+}$ are two of the most attractive mass produced commercial phosphors. It has been found that the upconversion brightness of $Y_2O_2S:Yb^{3+},Er^{3+}$ is 6.5 times that of $Y_2O_3:Yb^{3+},Er^{3+}$ [8]. Yocom et al. [9] demonstrated that $Y_2O_2S:Yb^{3+},Er^{3+}$ exhibited 82% brighter output than similar fluoride phosphors. Additionally, our recent studies [10] have demonstrated the application of $Gd_2O_2S:Yb^{3+},Er^{3+}$ as another potential candidate

* Corresponding author.
E-mail address: akgsh@yahoo.com (G.A. Kumar).

0925-8388/$ – see front matter © 2011 Elsevier B.V. All rights reserved.
doi:10.1016/j.jallcom.2011.11.006

for both up and down conversions. In this work, a solid-state flux fusion method was adopted to prepare fine $Y_2O_2S:Yb^{3+},Er^{3+}$ phosphor powders with hexagonal shape, narrow size distribution, and high luminescence efficiency. The luminescent spectral characteristic of $Y_2O_2S:Yb^{3+},Er^{3+}$ phosphors is investigated for a wide range of dopant compositions.

The crystal symmetry of Y_2O_2S is hexagonal with space group *P–3m1*. There is one formula unit per unit cell. The structure is very closely related to the *A*-type rare-earth oxide structure, the difference being that one of the three oxygen sites is occupied by a sulfur atom. Atomic positions in Y_2O_2S using lattice vector units are $\pm(1/3, 2/3, u)$ for two metal atoms with $u \sim 0.28$, $\pm(1/3, 2/3, v)$ for two oxygen atoms with $v \sim 0.63$, and (0, 0, 0) for a sulfur atom. Each metal atom is bonded to four oxygen atoms and three sulfur atoms to form a seven coordinated geometry with the oxygen and the metal in the same plane.

2. Experimental

A high temperature solid state flux fusion method was used for the phosphor syntheses. The starting materials are Y_2O_3, Yb_2O_3, Er_2O_3 (Sigma Aldrich, all 99.999%), S (powder) and Na_2CO_3, K_3PO_4 (Sigma Aldrich, 99.99%) as flux. Two different sets of samples were prepared with different $Yb^{3+}:Er^{3+}$ ratios. In the first series, the total $Yb^{3+} + Er^{3+}$ molar concentrations were fixed at 10 mol% viz. (0:10), (1:9), (2:8), (3:7), (5:5), (9:1), (9.5:0.5). In the second set, the Er^{3+} concentration was kept constant at 1 mol% while Yb^{3+} was varied and the $Yb^{3+}:Er^{3+}$ ratios were viz. (0:1), (1:1), (2:1), (3:1), (5:1), (9:1), (8:1). Both S and Na_2CO_3 were 30–50 wt% and K_3PO_4 was 20 wt%. The precursor materials were thoroughly mixed using agate mortar and pestle and then heated in a muffle furnace at 1150 °C for 60 min. The furnace was allowed to cool down and the samples were removed, washed with distilled water 6 times and then with a mild hydrochloric acid. The washed powder was subsequently dried and sieved.

The particle size was analyzed by a Coulter LS230 light scattering particle size analyzer. X-ray powder diffraction (XRD) was performed at 40 kV and 30 mA in the parallel beam configuration using a RIGAKU Ultima IV X-ray diffractometer with Cu Kα (λ = 1.5 Å). The morphology of the samples was observed using a Hitachi S5500 field emission scanning transmission electron microscope (FE-STEM) operated at 30 kV using secondary electrons.

The absorption spectra were measured in the 300–1700 nm range using a spectrophotometer (Cary Model 14R) in transmission mode. The emission spectra of the samples were recorded by exciting the sample using the 980 nm line of a continuous wave Ti:Sapphire laser (Spectra Physics Model 3900S) pumped by a frequency doubled $Nd^{3+}:YVO_4$ laser (Spectra Physics Millennia). The emission from the sample was collected with a 1.25 m single grating scanning monochromator (SPEX Model 1250M) and detected by a liquid nitrogen cooled InGaAs detector (Model DSS-1GA020L Electro-optic System Inc.) for the NIR and photo multiplier tube (Horiba Model 1911) for the visible. The fluorescence spectrum for NIR transitions was scanned using a 600 grooves/mm diffraction grating blazed at 1.5 μm and 1200 grooves/mm diffraction grating blazed at 0.5 μm for the visible region, with a spectral resolution of 0.01 nm. The NIR detector signal was processed in a PC coupled to the data acquisition system through a lock in amplifier (Stanford Research System Model SR510). The entire system was controlled though the data acquisition software Synergy (Origin Lab) and HORIBA (Jobin-Yvon). The decay profiles were recorded by pulsing the excitation laser with a chopper (Terahertz Technology Model C-995) and connecting the detector directly to a 100 MHz oscilloscope (Tektronix Model TDS 3012B). For comparison all samples were equally weighed and packed in cuvettes and excited with 20 mW of laser power. All the emission and decay time measurements were performed at room temperature. For color coordinate measurements an Ocean Optics (USB 4000) spectrometer was used in the emissive color mode at 2° observer angle. The FTIR spectrum was measured in transmission mode using the KBr method (Bruker, Model vector 22) and the Raman spectrum was obtained using Jobin-Yvon (Model iHR 320) spectrometer.

3. Results and discussion

3.1. Phase and morphology

The XRD data obtained for $Y_2O_2S:Yb^{3+},Er^{3+}$ is shown in Fig. 1, which is in agreement with standard powder peak positions of Y_2O_2S hexagonal phase (JCPDS Card No. 26-1422). The XRD results reveal that the well-crystallized $Y_2O_2S:Yb^{3+},Er^{3+}$ is hexagonal Y_2O_2S (*P–3m1*) phase with cell parameters $a = b = 0.3852$ nm, $c = 0.6567$ nm. According to the dynamic light scattering measurements (Fig. 2) the average particle size was estimated to be

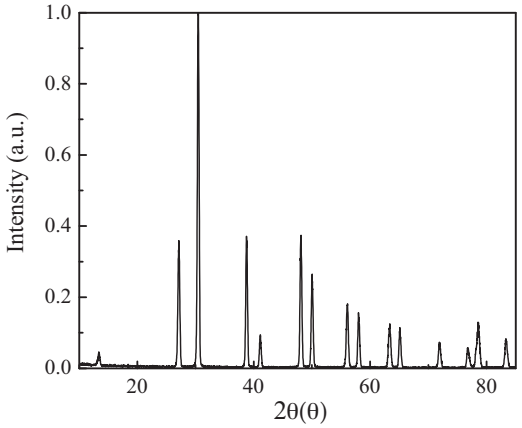

Fig. 1. XRD pattern of the $Y_2O_2S:Yb^{3+},Er^{3+}$ sample.

3.8 μm with a FWHM of 4.9 μm. It should be noted that the primary particle size of Y_2O_3 was reduced from 10 to 3.8 μm by flux fusion method. FE-STEM micrographs obtained from different locations show that the material is predominantly crystallized in a hexagonal shape. Analysis of the elemental composition by EDS shows the wt% of various elements inside the composition $Y_2O_2S:Yb^{3+}(2),Er^{3+}(1)$ as $Y_{final} = 42.5\%$, $Yb_{final} = 2.53\%$, $Er_{final} = 1.05\%$ and $S_{final} = 7.46\%$ which is in agreement with the starting composition $Y_{start} = 42.2\%$, $Yb_{start} = 2.3\%$ and $Er_{start} = 0.74\%$. The S content in the final composition is found to be less than the starting composition ($S_{start} = 22.62\%$) and may be explained by the excess oxidation rate of elemental sulfur during the firing process.

3.2. Radiative properties

The room temperature UV–VIS–NIR absorption spectrum of the sample given in Fig. 3 consists of several well resolved absorption bands with their spectral width and band positions comparable with those of the standard Yb^{3+}/Er^{3+} spectrum. The absorption bands of the Er^{3+} ions correspond to transitions from the $^4I_{15/2}$ ground state to the various excited levels. The data from these absorption spectra has been used to calculate the radiative transition probabilities, fluorescence branching ratios and radiative lifetimes of various transitions using a standard least-square fitting procedure [11–13]. The experimental and calculated electric dipole line strengths of the different absorption bands observed are collected in Table 1 along with the RMS deviation of the fit. The Judd–Ofelt parameters obtained for the Er^{3+} in the present system are $\Omega_2 = 3.40 \times 10^{-20}$ cm^2, $\Omega_4 = 4.28 \times 10^{-20}$ cm^2,

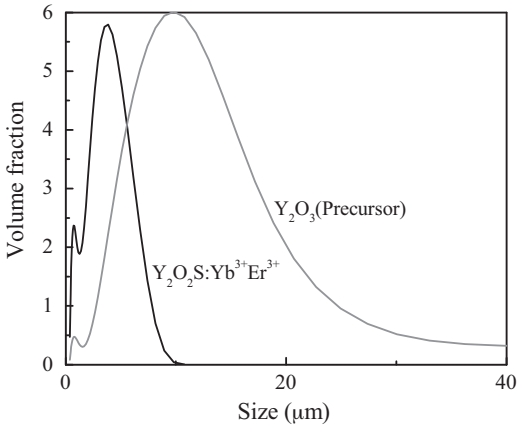

Fig. 2. Particle size distribution from dynamic light scattering measurements.

Table 1
Measured and calculated absorption line strengths of Er^{3+} in Er^{3+}/Yb^{3+} co-doped Y_2O_2S.

Transition (from $^4I_{15/2}$)	λ (nm)	S_{meas} (10^{-20} cm^2)	S_{calc}[a] (10^{-20} cm^2)	$(\Delta S)^2$ (10^{-40} cm^4)
$^4I_{13/2}$	1532	1.829	1.828	0.000
$^4I_{9/2}$	805	0.741	0.750	0.000
$^4F_{9/2}$	660	2.751	2.698	0.003
$^4S_{3/2}$	548	0.297	0.194	0.011
$^2H_{11/2}$	523	4.266	4.266	0.000
$^4F_{7/2}$	492	0.999	1.180	0.032
$^4F_{5/2} + {}^4F_{3/2}$	458	0.492	0.308	0.034

[a] Fitting parameters $\Omega_2 = 3.40 \times 10^{-20}$ cm^2, $\Omega_4 = 4.28 \times 10^{-20}$ cm^2, $\Omega_6 = 0.88 \times 10^{-20}$ cm^2, ΔS RMS error $= 0.14 \times 10^{-20}$ cm^2.

Table 2
Predicted fluorescence line strengths (S_{calc}), radiative decay rates (A), and branching ratios (β) of Er^{3+}/Yb^{3+} co-doped Y_2O_2S at 300 K.

Transition	λ (nm)	n	S_{calc} (10^{-20} cm^2)	A (s^{-1})	β	τ_{rad} (ms)
$^4I_{13/2} \rightarrow {}^4I_{15/2}$	1511	2.1	1.828	303	1.000	3.29
$^4I_{11/2} \rightarrow {}^4I_{13/2}$	2778	2.1	1.799	48	0.155	
$^4I_{11/2} \rightarrow {}^4I_{15/2}$	990	2.21	0.445	265	0.845	3.182
$^4I_{9/2} \rightarrow {}^4I_{11/2}$	4651	2.1	0.411	3	0.002	
$^4I_{9/2} \rightarrow {}^4I_{13/2}$	1739	2.1	0.677	89	0.072	
$^4I_{9/2} \rightarrow {}^4I_{15/2}$	816	2.23	0.750	1144	0.925	0.809
$^4F_{9/2} \rightarrow {}^4I_{9/2}$	3448	2.1	0.484	8	0.001	
$^4F_{9/2} \rightarrow {}^4I_{11/2}$	1980	2.1	1.416	127	0.015	
$^4F_{9/2} \rightarrow {}^4I_{13/2}$	1156	2.1	0.753	339	0.041	
$^4F_{9/2} \rightarrow {}^4I_{15/2}$	660	2.26	2.698	3784	0.943	0.234
$^4S_{3/2} \rightarrow {}^4F_{9/2}$	3125	2.1	0.025	1	0.000	
$^4S_{3/2} \rightarrow {}^4I_{9/2}$	1639	2.1	0.561	221	0.058	
$^4S_{3/2} \rightarrow {}^4I_{11/2}$	1212	2.1	0.083	81	0.021	
$^4S_{3/2} \rightarrow {}^4I_{13/2}$	844	2.24	0.305	671	0.177	
$^4S_{3/2} \rightarrow {}^4I_{15/2}$	553	2.27	0.194	2812	0.743	0.264

$\Omega_6 = 0.88 \times 10^{-20}$ cm^2. These values are in excellent agreement with the values reported earlier for $Y_2O_2S:Er^{3+}$ (1%) single crystals [14]. The values of the radiative transition probabilities for the most common emission bands are shown in Table 2 along with the estimated fluorescence branching ratios (β) and radiative decay times (τ_{rad}). Using the calculated radiative transition probabilities of the emission bands and their measured spectral widths, the emission cross sections (σ_e) can be obtained from the emission data [12]. Using this procedure the emission cross sections obtained for various observed emission bands are 0.521×10^{-20} cm^2 (555 nm), 1.17×10^{-20} cm^2 (672 nm) and 2.62×10^{-20} cm^2 (1511 nm). It should be noted that these cross sections are approximately 4 times higher than other crystalline [15] hosts and more than 8 times higher than other amorphous [16] host materials. These large values are mainly due to the low effective line width and the high radiative transition probability, both of which can be beneficial in achieving intense emission with high gain.

3.3. Infrared and upconversion luminescence spectra

Fig. 4 shows the infrared emission of the phosphor, where the peak emission was observed at 1511 nm with a spectral bandwidth of 18 nm. Fig. 5 and its inset show a 980 nm excited upconversion spectrum for $Y_2O_2S:Yb^{3+}(8),Er^{3+}(1)$ in the 400–850 nm range. In the 400–500 nm range there is a comparatively stronger emission at 410 nm. The emission spectrum in the 500–700 nm range is characterized by an intense green band at 555 nm followed by a weaker red band at 672 nm. In the 750–850 nm range the main emission was observed at 820 nm. All of these emission bands are accompanied by several well resolved Stark levels. The fluorescence branching ratios of the green and red upconversion bands are 49.5% and 48.31% respectively. Since the intensities are comparable the samples glow with yellow color due to color mixing. The upconversion in these samples can be observed with the naked eye at an excitation power less than 15 μW. Due to the brightness of the emission, 20 mW of excitation power was used in all experiments.

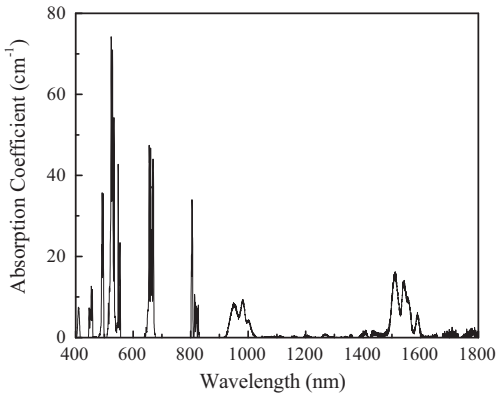

Fig. 3. Optical absorption spectrum of $Y_2O_2S:Yb^{3+}(1),Er^{3+}(9)$ phosphor.

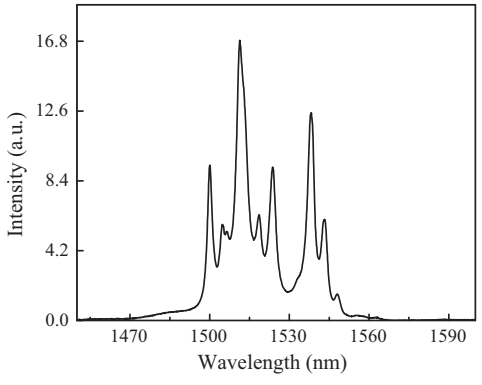

Fig. 4. Infrared emission spectrum of $Y_2O_2S:Yb^{3+}(8),Er^{3+}(1)$ phosphor under 980 nm laser excitation.

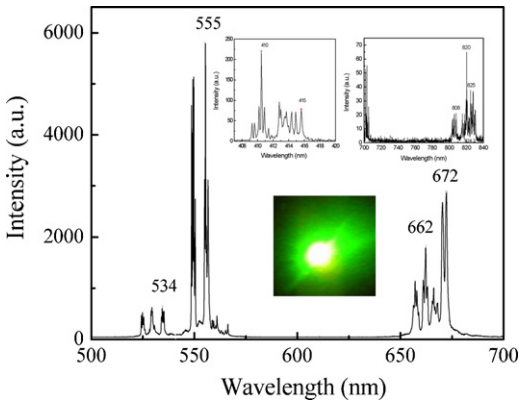

Fig. 5. Upconversion emission spectrum of Y_2O_2S:Yb^{3+}(9),Er^{3+}(1) phosphor under 980 nm laser excitation in the 400–850 nm range. Inset shows the photograph of the green emission under 20 mW excitation power.

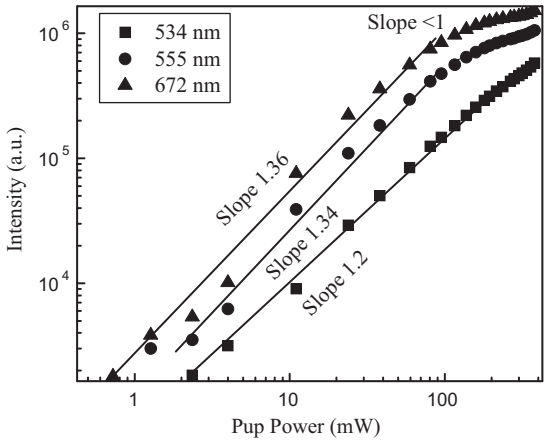

Fig. 7. Dependence of the excitation power on the emission intensity of green and red emissions.

The inset of Fig. 5 shows a photograph of the green upconversion emission upon 20 mW excitation at 980 nm.

The upconversion process in the Yb^{3+}–Er^{3+} system is well understood in several materials [17,18] and is briefly explained in the energy level diagram shown in Fig. 6. Emission bands observed at 410, 492, 534, 555, 672, 820 and 1511 nm are assigned to the $^2H_{9/2} \rightarrow {}^4I_{15/2}$, $^4F_{7/2} \rightarrow {}^4I_{15/2}$, $^2H_{11/2} \rightarrow {}^4I_{15/2}$, $^4S_{3/2} \rightarrow {}^4I_{15/2}$, $^4F_{9/2} \rightarrow {}^4I_{15/2}$, $^4I_{9/2} \rightarrow {}^4I_{15/2}$ and $^4I_{13/2} \rightarrow {}^4I_{15/2}$ transitions respectively. The appearance of the blue, green and red emission bands can be explained on the basis of various processes such as two photon absorption (TPA), excited state absorption (ESA) and energy transfer (ET). TPA is a nonlinear process where the visible photons are created by the simultaneous absorption of two photons and mediated through a real or virtual intermediate level. TPA is relevant when excitation light sources being used have high power that is sufficient enough to create virtual intermediate levels in materials with high TPA cross section. In the case of trivalent Er^{3+}, TPA can occur through the real states due of the presence of matching energy levels. When the $^4I_{11/2}$ level is excited by 980 nm directly through Er^{3+} or through Yb^{3+} excitation photons, part of the excitation energy at the $^4I_{11/2}$ level relaxes non-radiatively to the $^4I_{13/2}$ level giving rise to the $^4I_{13/2} \rightarrow {}^4I_{15/2}$ emission. At the same time, the populated $^4I_{11/2}$ level is excited to the $^4F_{7/2}$ state by ESA of a second photon. From the $^4F_{7/2}$ level another 980 nm photon can be absorbed to an equally similar excited level. As explained earlier, these excited state processes can happen equally under high photon density through nonlinear absorption processes such as two photon or three photon absorption. After these excited state processes, de-excitation populates the electrons in different excited states and the intensity of emission depends on the electron density at that particular level as well as the non-radiative contribution to the emission band. The population accumulated in the $^2H_{9/2}$ level gives the 410 nm emission by radiatively decaying to $^4I_{15/2}$. Since the efficiency of this third order process is less than the two photon process, the emission intensity of the 410 nm band is comparatively weak. On the other hand, the two photon processes that populate the $^4F_{7/2}$ level is so efficient that it can give very efficient green emission transitions from $^2H_{11/2}$ level due to the fast multi-phonon non-radiative decay of $^4F_{7/2}$ level to $^2H_{11/2}$. Because of several closely spaced levels in between $^2H_{11/2}$ and $^4S_{3/2}$, multi-phonon relaxation results in decaying the $^2H_{11/2}$ level to $^4S_{3/2}$ yielding the strongest emission band at 555 nm. The decay time of the $^4S_{3/2}$ level was measured to be 163 μs which is sufficient to make this as a meta-stable level for the green emission. Further, since the energy gap between $^4S_{3/2}$ and $^4F_{9/2}$ is 2800 cm^{-1} multi-phonon relaxation is unlikely to happen and hence the $^4S_{3/2} \rightarrow {}^4F_{9/2}$ transition could be radiative.[1] Part of the population decaying to the $^4F_{9/2}$ level can result in the red emission at 672 nm through the $^4F_{9/2} \rightarrow {}^4I_{15/2}$ transition. Fractional population accumulated in $^4I_{9/2}$ level gives rise to the 820 nm emission through $^4I_{9/2} \rightarrow {}^4I_{15/2}$ transition. Finally, the emission from $^4I_{13/2}$ level, being a metastable level with lifetime of 3.2 ms, gives the most intense 1511 nm emission band. The major process that populates the $^4F_{9/2}$ level of Er^{3+} is the energy transfer process from Yb^{3+} according to the relation $^2F_{5/2}(Yb^{3+}) + {}^4I_{13/2}(Er^{3+}) \rightarrow {}^2F_{7/2}(Yb^{3+}) + {}^4F_{9/2}(Er^{3+})$.

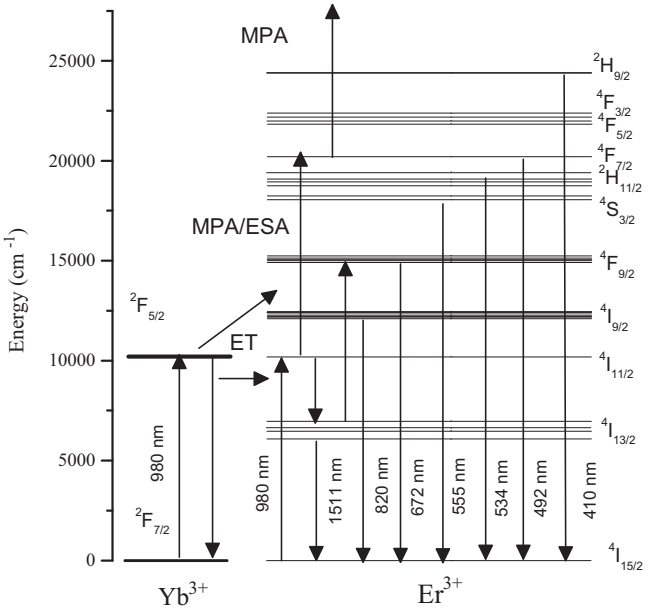

Fig. 6. Energy level diagram of Yb^{3+}–Er^{3+} system showing possible excitation and de-excitation mechanism under 980 nm excitation. MPA, multiphoton absorption; ET, energy transfer.

In order to establish the presence of these nonlinear processes, the pump power dependence of the emission bands on the emission intensity was measured and the relationship obtained is plotted in Fig. 7 for 534, 555 and 672 nm emission peaks. The log–log plot of the emission intensity vs the incident pump power determines the number of photons involved for a given emission band viz. $I \sim P^n$ where I is the emission intensity, P is the incident pump power, and n is the number of photons involved. In a typical experiment

[1] We observed 3.2 μm emission through the $^4S_{3/2} \rightarrow {}^4F_{9/2}$ transition.

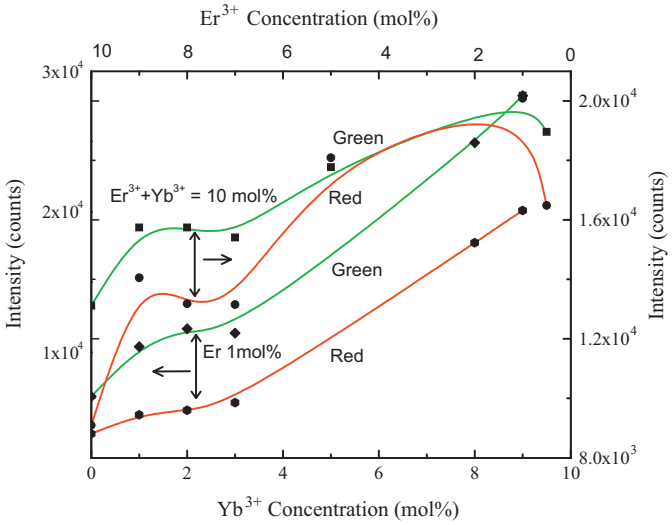

Fig. 8. Variation of green and red emission intensities as a function of Yb concentration at fixed Er concentration at 1 mol% and fixed Er^{3+} + Yb^{3+} concentration at 10 mol%.

the measured slope (i.e. the number of photons involved in a transition) is rounded up to the nearest integer. In our experiments we measured the emission intensities up to 100 mW excitation power, the slopes measured for the 534, 555 and 672 nm emission peaks are 1.20, 1.34, and 1.36, respectively, suggesting that the upconversion is a two photon process. It is interesting to note that the present material shows upconversion under normal 980 nm filtered Xe lamp excitation which corroborates the fact that in this composition ESA also contributes to the upconversion process. The fact that the material shows intense upconversion under low power excitation shows that the efficiency of upconversion in this material is comparatively higher. Furthermore, under high power excitation the material shows almost a linear relationship between the log of the intensity vs the log of the pump power which is likely due to excitation population saturation at high excitation power.

In order to understand the functional dependence of the red and green emission intensities on the Yb^{3+} concentrations, two sets of samples were prepared. In the first set, the Yb^{3+}–Er^{3+} concentration was kept fixed at 10 mol% by proportionally changing Yb^{3+} and Er^{3+} concentrations. In the second set, the Yb^{3+} concentration was varied from 0 to 9 mol% while keeping the Er^{3+} concentration constant at 1 mol%. Results of both experiments are presented in Fig. 8. In the case of samples with constant Er^{3+} concentration, both green and red emission intensities increase with the concentration of Yb^{3+} with green emission stronger than the red. However, for varying Er^{3+} concentration, both red and green manifolds exhibit peaks at 8 mol% of Yb^{3+} and 2 mol% of Er^{3+} as shown in Fig. 8.

The excitation saturation at comparatively low power excitation is particularly useful in several photonics applications such as solar energy converter or laser amplifier where high power excitation was required to achieve the desired energy conversion. With comparatively low power excitation efficient upconversion phosphor layers, it may be possible to enhance the energy conversion efficiency of the Si solar cells. The same concept applies to the development of low pump threshold solid state lasers, ceramic lasers and fiber amplifiers created with similar phosphor compositions. As a continuation of this work we are in the process of measuring the external quantum efficiency of the 980/1550 nm to visible and NIR emission in these materials as a function of the compositions with the intention of using them in our current solar cell project.

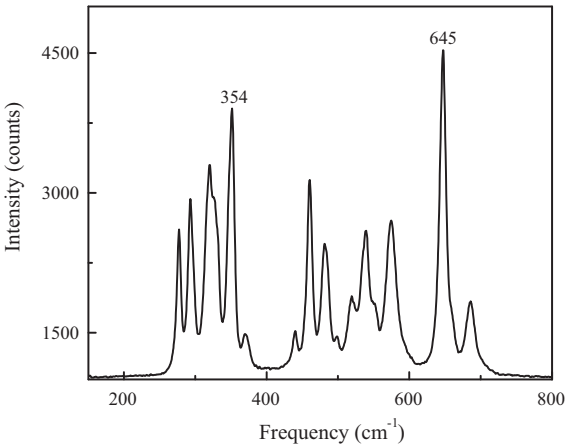

Fig. 9. Raman spectrum of Y_2O_2S:Yb^{3+}(8),Er^{3+}(1) phosphor.

3.4. Non-radiative processes and internal quantum yield

A quantitative way of measuring the internal quantum yield for a particular emission band is done through the fluorescence lifetime measurements. Non-radiative processes such as multiphonon relaxation, vibrational losses by surface (such as hydroxyl) species and energy transfer interactions quench the fluorescence intensity and the efficiency. The observed lifetime of the emission can be written as [5]:

$$\frac{1}{\tau_{lum}} = A_{rad} + W_{mp} + W_{OH} + W_{ET}, \quad (1)$$

where A_{rad}, W_{mp}, W_{OH}, W_{ET} are the radiative transition rate, transition rate from multiphonon relaxation, hydroxyl groups and energy transfer interaction respectively. The main contribution to non-radiative decay comes from multi-phonon relaxation from the host and energy transfer interactions between nearby ions. The transition probability by energy transfer is dependent on the distance between the donor (D) and acceptor (A) ions, R_{DA}, and hence dependent on the concentration of the ions. When the ions are homogeneously distributed in the matrix, the energy transfer relaxation rate W_{ET} can be written as [19]:(2)$W_{ET} \propto \frac{1}{R_{DA}^6} \propto N^2$, where N is the dopant concentration. On the other hand, the radiative transition probabilities and multi-phonon relaxation rates do not depend on the dopant concentration. The values of W_{OH} and W_{mp} can be determined from quantitative measurements of the OH content and from the low frequency vibrational modes in the sample measured from the infrared Raman spectrum shown in Fig. 9. The Raman spectrum shows the characteristic Y–O and Y–S symmetric vibration at 645 and 354 cm^{-1}. Using this frequency the multi-phonon vibrational loss of the 1511 nm emission band was estimated to be 0.00246 cm^{-1}.

The presence of water content in the sample is confirmed by the absorption band at 3439 cm^{-1} in the IR spectrum shown in Fig. 10. The absolute measurement of OH content is difficult, particularly at concentrations below 1000 ppm. However, a relative estimate of the water content can be obtained from the infrared absorption measurements corresponding to the OH band. The amount of water content in the samples can be obtained from the measurement of the absorption coefficient at the OH peak of the IR spectrum and is estimated to be nearly 2.5 cm^{-1}. An OH concentration of 360 ± 100 ppm gives absorption of ~2.8 cm^{-1} [20]. By comparison, the corresponding water content was estimated to be 327 ppm (5.8×10^{19} molecules/cm^3). Since the second order vibrational frequency of OH is almost in resonance with the $^4I_{13/2} \rightarrow {}^4I_{15/2}$ transition in Er^{3+} they are powerful quenchers of the Er^{3+} emission at 1511 nm. The quenching rate due to this water

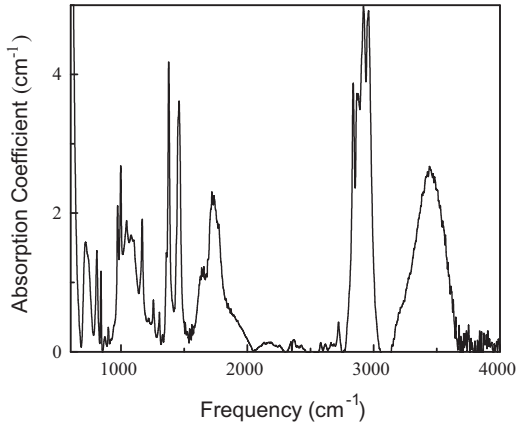

Fig. 10. FTIR vibrational spectrum of $Y_2O_2S:Yb^{3+}(8),Er^{3+}(1)$ phosphor.

content is found to be proportional to the absorption coefficient of the OH radicals [21]. The major sources of OH content in the phosphor are from the starting chemicals as well as from the atmosphere during synthesis. A higher level of water content can be suppressed by using moisture free chemicals melted in water free environment as well as the re-firing the material.

The internal quantum efficiency (η_{Int}) can be evaluated from the ratio of the fluorescence lifetime to radiative decay time [12]. The fluorescence lifetime obtained for the 555 and 1511 nm emission bands is 163 μs and 3.2 ms respectively. This gives an internal quantum yield of 61.7 and 97.3% for the 555 and 1511 nm emission bands, respectively.

3.5. CIE color coordinates analysis

To measure the color of the visible emission, color coordinates (x,y,z) were calculated from the (X,Y,Z) tri-stimulus values using standard procedure [22].

In addition, using the color coordinates calculated above, the correlated color temperatures (CCTs) of the mixed upconversion fluorescence corresponding to different excitation powers were given by the McCamy empirical formula [23]

$$CCT = -437n^3 + 3601n^2 - 6861n + 5514.31, \quad (3)$$

where $n = (x - x_e)/(y - y_e)$ is the inverse slope line, and $x_e = 0.3320$ and $y_e = 0.1858$ [23]. The color coordinates and CCT under different excitation powers are listed in Table 3, and the color coordinates are marked in Fig. 11 for the brightest composition. The power dependence of both x and y coordinates is plotted in Fig. 12 (left Y axis). The x CIE coordinates can be fitted with a parabolic function of the form $x = A + BP + CP^2$ where $A = 0.2385$, $B = 0.00325$ and $C = 0.00002$. The y coordinate assumes the shape of a function of the form

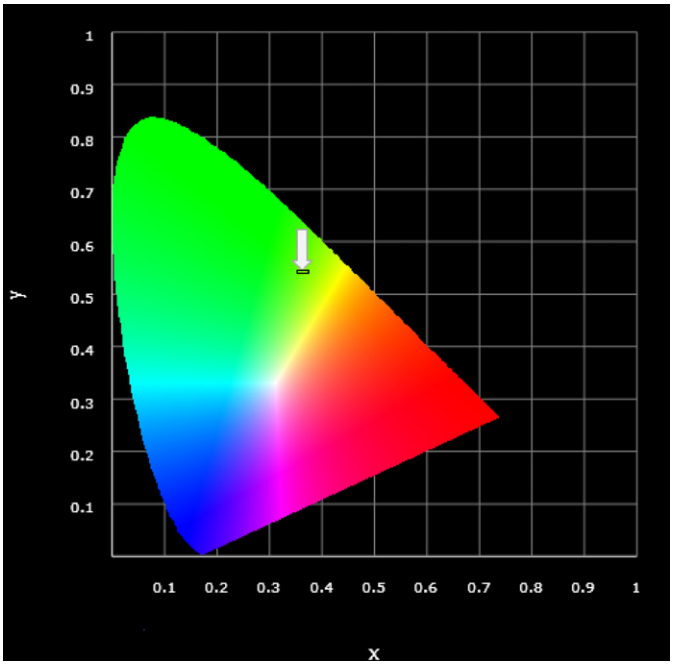

Fig. 11. CIE color coordinate plot showing the x, y coordinates of the emission in $Y_2O_2S:Yb^{3+}(8),Er^{3+}(1)$. The emission color was marked by the white arrow.

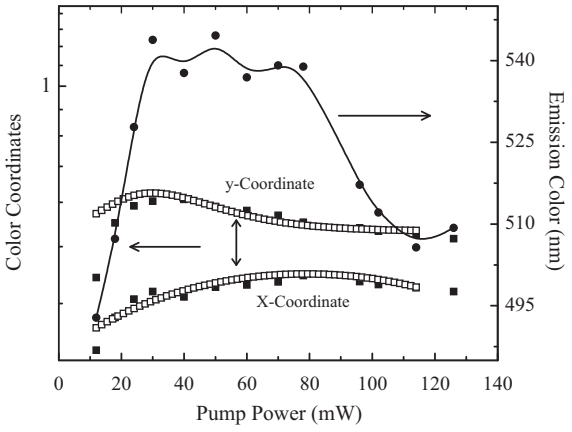

Fig. 12. Functional dependence of the 980 nm excitation power on x, y color coordinates in $Y_2O_2S:Yb$ (8),Er (1) and power dependent emission color tuning in $Y_2O_2S:Yb$ (8),Er (1) phosphor.

$y = y_0 + Ae^{(-e^{(-z)}-z+1)}$ where $z = (P - Pc)/w$ with $y_0 = 0.48$, $Pc = 30$, $w = 17$ and $A = 0.1025$. The power dependence shows that the x-coordinate increases with power up to 80 mW and then decreases. On the other hand the y-coordinate exhibits increasing tendency

Table 3
CIE (x,y,z), (X,Y,Z) color coordinates, color temperature (CCT) and color purity of $Y_2O_2S:Yb^{3+}(9),Er^{3+}(1)$ for different excitation power.

Power (mW)	Dominant color (nm)	X	Y	Z	x	y	z	CCT (K)	Purity
12	492.8	84.3	121.73	114.31	0.2632	0.3800	0.3568	8374	0.448
18	507.3	384.86	620.71	233.74	0.3105	0.5009	0.1886	6002	0.313
24	527.8	1110.24	1779.05	368.80	0.3408	0.5460	0.1132	5380	0.338
30	543.8	2082.47	3288.17	510.20	0.3541	0.5591	0.0868	5159	0.446
40	537.7	2456.41	4025.83	650.07	0.3444	0.5644	0.0911	5327	0.434
50	544.6	3060.82	4602.87	790.55	0.3620	0.5444	0.0935	5006	0.398
60	536.9	3219.72	4689.92	886.95	0.3660	0.5332	0.0100	4919	0.352
70	539.1	3421.59	4789.29	993.99	0.3717	0.5203	0.1080	4793	0.305
78	538.9	3778.09	4947.62	1118.24	0.3838	0.5026	0.1136	4529	0.258
96	517.2	3843.5	5038.75	1439.69	0.3724	0.4882	0.1395	4701	0.194
102	512.1	3879.49	5083.16	1618.0	0.3667	0.4804	0.1529	4794	0.193
114	505.7	3916.98	5133.24	1799.66	0.3610	0.4731	0.1659	4893	0.199
126	509.3	3969.36	5190.07	2060.36	0.3538	0.4626	0.1836	5029	0.212

only for powers of up to 30 mW and thereafter decreases continuously. The color tuning range of the phosphor is shown in Fig. 12 (right *Y* axis) where it can be seen that the emission color can simply be tuned from 490 nm to 545 nm by changing the excitation power from 10 to 50 mW.

The power dependent color tuning possibility of the present phosphor material could find variety of applications such as tunable upconversion ceramic lasers, color tunable phosphor coatings, multi-color biomedical imaging materials, 3D displays, infrared activated LED design as well as in polymer fiber lasers and planar waveguides. Recently we successfully made nanoparticles of several oxysulfide upconversion phosphors and are currently investigating the optical properties of these nanoparticles in several fluoropolymers with the intention of producing optical fibers and planar waveguide structures for low pump threshold upconversion laser applications.

4. Conclusions

Using the solid state flux fusion method hexagonal shaped $Y_2O_2S:Yb^{3+},Er^{3+}$phosphors were synthesized and their UV–VIS–NIR spectroscopic properties were studied for a range of Yb^{3+} and Er^{3+} dopant concentrations. Analysis shows that at 9 mol% Yb^{3+} and 1 mol% Er^{3+} the phosphor exhibits the brightest green emission. The upconversion efficiency in this material is high enough that with less than 15 μW of 980 nm excitation power one could observe the green upconversion with the naked eye. The internal quantum yields of the green emission at 555 nm and infrared emission at 1511 nm are 67 and 97%, respectively. The low power excitation upconversion mechanism in this material offers several potential applications such as solar energy conversion and low threshold upconversion lasers. In addition, the material offers power dependent color tuning properties where the emission color can be tuned from 490 nm to 545 nm by simply changing the 980 nm excitation power from 10 to 50 mW. Upconversion color tunability by changing the pump power intensity offers prospects of several diverse photonics applications such as novel three-dimensional solid-state displays, upconversion LED lighting, biomedical multi-color imaging, lasers and many more.

Acknowledgements

This work was supported by the National Science Foundation Partnerships for Research and Education in Materials (NSF-PREM) Grant No. DMR-0934218. Martinez acknowledges the support from FONCICYT through Grant No. 94142.

References

[1] M. Wang, G. Abbineni, A. Clevenger, C. Mao, S. Xu, Nanomedicine: Nanotechnol. Biol. Med., in press.
[2] G. Dong, B. Wu, F. Zhang, L. Zhang, M. Peng, D. Chen, E. Wu, J. Qiu, J. Alloys Compd. 509 (2011) 9335.
[3] Q. Liu, M. Chen, Y. Sun, G. Chen, T. Yang, Y. Gao, X. Zhang, F. Li, Biomaterials 32 (2011) 8243.
[4] S.C. Prashantha, B.N. Lakshminarasappa, B.M. Nagabhushana, J. Alloys Compd. 509 (2011) 10185.
[5] W. Chen, Doped Nanomaterials and Nanodevices, American Scientific Publishers, Stevenson Ranch, CA, 2010.
[6] B. Di Bartolo, G. Armagan, Spectroscopy of Solid-state Laser-type Materials, International School of Atomic and Molecular Spectroscopy, Plenum Press, New York, 1989.
[7] G.F.J. Garlick, C.L. Richards, J. Lumin. 9 (1974) 432.
[8] X. Luo, W. Cao, Sci. China Ser. B: Chem. 50 (2007) 505.
[9] P. Yocom, J. Wittke, I. Ladany, Metall. Mater. Trans. B 2 (1971) 763.
[10] G.A. Kumar, M. Pokhrel, D.K. Sardar, Opt. Mater. Express (2011).
[11] B.R. Judd, Phys. Rev. 127 (1962) 750.
[12] A.A. Kaminskii, Laser Crystals: Physics and Properties, Springer-Verlag, Berlin/New York, 1979.
[13] G. Ofelt, J. Chem. Phys. 37 (1962) 511.
[14] S. Buddhudu, F.J. Bryant, J. Less Common Met. 147 (1989) 213.
[15] L. Han, Appl. Phys. Lett. 93 (2008) 011110.
[16] F. Gan, Optical and Spectroscopic Properties of Glass, Springer-Verlag, 1992.
[17] P.C. Becker, N.A. Olsson, J.R. Simpson, Erbium-doped Fiber Amplifiers: Fundamentals and Technology, Academic Press, San Diego, 1999.
[18] M.J.F. Digonnet, Society of Photo-optical Instrumentation, Selected Papers on Rare-earth-doped Fiber Laser Sources and Amplifiers, SPIE Optical Engineering Press, Bellingham, WA, 1992.
[19] D. Dexter, J. Chem. Phys. 21 (1953) 836.
[20] D.E. Day, J.M. Stevels, J. Non-Cryst. Solids 14 (1974) 165.
[21] S.A. Payne, M.L. Elder, J.H. Campbell, G.D. Wilke, M. Weber, J. Am. Ceram. Soc. 28 (1991) 253.
[22] http://en.wikipedia.org/wiki/CIE_1931_color_space.
[23] C.S. McCamy, Color Res. Appl. 17 (1992) 142.